Room-temperature performance of 3 mm-thick cadmium–zinc–telluride pixel detectors with sub-millimetre pixelization

Antonino Buttacavoli,[a] Fabio Principato,[a] Gaetano Gerardi,[a] Manuele Bettelli,[b] Nicola Sarzi Amadè,[b] Andrea Zappettini,[b] Paul Seller,[c] Matthew C. Veale,[c] Oliver Fox,[d] Kawal Sawhney[c] and Leonardo Abbene[a]*

[a]Department of Physics and Chemistry (DiFC) – Emilio Segrè, University of Palermo, Viale delle Scienze, Edificio 18, 90128 Palermo, Italy, [b]IMEM/CNR, Parco Area delle Scienze 37/A, 43100 Parma, Italy, [c]Science and Technology Facilities Council, Rutherford Appleton Laboratory, Chilton, Oxfordshire OX11 0QX, United Kingdom, and [d]B16 Beamline, Diamond Light Source, Fermi Avenue, Didcot, United Kingdom. *Correspondence e-mail: leonardo.abbene@unipa.it

Cadmium–zinc–telluride (CZT) pixel detectors represent a consolidated choice for the development of room-temperature spectroscopic X-ray imagers, finding important applications in medical imaging, often as detection modules of a variety of new SPECT and CT systems. Detectors with 3–5 mm thicknesses are able to efficiently detect X-rays up to 140 keV giving reasonable room-temperature energy resolution. In this work, the room-temperature performance of 3 mm-thick CZT pixel detectors, recently developed at IMEM/CNR of Parma (Italy), is presented. Sub-millimetre detector arrays with pixel pitch less than 500 μm were fabricated. The detectors are characterized by good room-temperature performance even at high bias voltage operation (6000 V cm^{-1}), with energy resolutions (FWHM) of 3% (1.8 keV) and 1.6% (2 keV) at 59.5 keV and 122.1 keV, respectively. Charge-sharing investigations were performed with both uncollimated and collimated synchrotron X-ray beams with particular attention to recovering the charge losses at the inter-pixel gap region. High rate measurements demonstrated the absence of high-flux radiation-induced polarization phenomena up to 25×10^6 photons mm^{-2} s^{-1}.

1. Introduction

Nowadays, cadmium zinc telluride (CdZnTe or CZT) is a consolidated semiconductor material for room-temperature radiation detection (Del Sordo *et al.*, 2009; Johns & Nino, 2019; Owens & Peacock, 2004; Takahashi & Watanabe, 2001). The success of this compound semiconductor for X-ray and gamma ray detection, aside from its appealing physical properties (high atomic number, wide band gap, high density), can mainly be attributed to the important advancements of crystal growth and device fabrication technologies (Abbene *et al.*, 2016, 2020; Chen *et al.*, 2008; Iniewski, 2014; Prokesch *et al.*, 2018; Szeles *et al.*, 2008; Zappettini *et al.*, 2009). Currently, the best spectroscopic-grade CZT crystals are fabricated using the travelling heater method (THM) growth technique (Chen *et al.*, 2008; Iniewski, 2014; Prokesch *et al.*, 2018; Veale *et al.*, 2020). If compared with other high-Z and wide-bandgap compound semiconductors (Del Sordo *et al.*, 2009; Owens & Peacock, 2004), the charge transport properties of THM-grown CZT crystals are very impressive, with mobility-lifetime products of electrons $\mu_e\tau_e$ greater than 10^{-2} cm^2 V^{-1}. However, aside from the characteristics of the crystals, the electrical contacts of the detectors also play a crucial role. In general, the electrical contacts of a detector should ensure
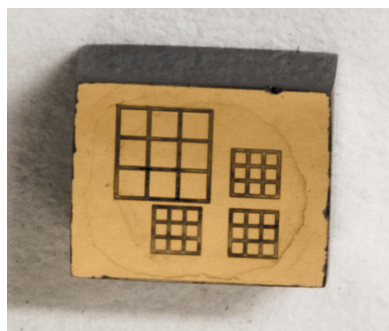
high bias voltage operation to optimize the charge collection process and, at the same time, maintain the leakage currents (*i.e.* the related electronic noise) to be as low as possible. Typically, CZT detectors are fabricated with quasi-ohmic electrical contacts (gold, platinum), allowing electric fields greater than 3000 V cm^{-1} (Chen *et al.*, 2008; Iniewski, 2014; Prokesch *et al.*, 2018), a moderate leakage current ($<$20 nA cm^{-2} at 1000 V cm^{-1}) (Awadalla *et al.*, 2014; Bell *et al.*, 2015) and no bias-induced polarization phenomena (Farella *et al.*, 2009; Principato *et al.*, 2013; Turturici *et al.*, 2014).

Recently, THM-grown CZT detectors with high bias voltage operation were fabricated at IMEM/CNR of Parma (Italy) (Abbene *et al.*, 2017*a,b*). Planar CZT samples with customized gold electroless contacts were realized, ensuring low leakage currents ($<$5 nA cm^{-2} at 1000 V cm^{-1}) and good room-temperature operation even at high bias voltages ($>$5000 V cm^{-1}) (Abbene *et al.*, 2017*a,b*). As a further step, we developed new THM-grown CZT pixel detectors with sub-millimetre pixelization. The detectors, with pixel pitches of 500 μm and 250 μm, are characterized by a thickness of 3 mm, which is appealing as it enables us to efficiently detect X-rays up to 140 keV. Several research groups have recently focused on the development of 3 mm-thick CZT pixel detectors for energy-resolved X-ray imaging (Barber *et al.*, 2015; Brambilla *et al.*, 2012, 2013; Del Sordo *et al.*, 2004, 2005; Iwanczyk *et al.*, 2009).

The aim of this work is to present the room-temperature performance of these new CZT pixel detectors, recently developed at IMEM/CNR Parma, Italy. The detector signals were amplified with low-noise preamplifiers (ASIC) and processed with multichannel digital electronics. Spectroscopic investigations with both uncollimated and collimated X-ray beams were performed, with particular attention given to the charge-sharing and charge-loss effects in the energy spectra.

2. Detectors and electronics

CZT pixel detectors with a thickness of 3 mm were realized at IMEM/CNR (Parma, Italy; http://www.imem.cnr.it). The detectors were fabricated from commercial CZT crystals (provided by Redlen Technologies, Victoria, BC, Canada) grown by the THM technique. As is well known (Chen *et al.*, 2008; Iniewski, 2014), Redlen (http://redlen.ca) is able to produce spectroscopic-grade CZT crystals with excellent charge-transport properties (mobility-lifetime products of electrons $\mu_e\tau_e > 10^{-2}$ cm^2 V^{-1}). In this work, we used CZT crystals characterized by $\mu_e\tau_e$ ranging from 1×10^{-2} cm^2 V^{-1} to 3×10^{-2} cm^2 V^{-1} (Abbene *et al.*, 2017*a*). Gold electroless contacts were realized on both the anode (prepared using water solutions) and the cathode (prepared using alcoholic solutions) of all CZT samples (Benassi *et al.*, 2017; Marchini *et al.*, 2009). As shown in Fig. 1, four arrays of 3 × 3 pixels with pixel pitches of 500 μm and 250 μm were created on the anode surface; the arrays are surrounded by a guard-ring electrode, while the cathode is a planar electrode covering the detector surface. The width of the inter-pixel gaps for all arrays is equal
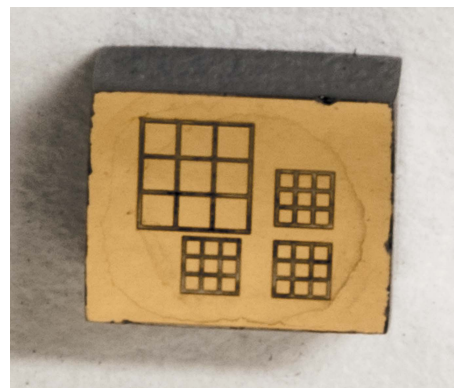
Figure 1
Photograph of a 3 mm-thick THM-grown CZT detector (anode side-view). The four arrays of 3 × 3 pixels with pixel pitches of 500 μm and 250 μm are clearly visible.

to 50 μm. Two detectors with the same anode and cathode geometry were developed and tested, showing similar spectroscopic performance.

The pixels of the detectors were DC-coupled to analog charge-sensitive preamplifiers (CSPs) and processed by multichannel digital pulse processing (DPP) electronics. A low-noise ASIC (PIXIE ASIC), developed at RAL (Didcot, UK) (Allwork *et al.*, 2012; Veale *et al.*, 2011), was flip-chip bonded directly to the detector pixels. The bonding process was performed at RAL by low-temperature curing ($<$150°C) silver-loaded epoxy and the gold stud bonding technique (Schneider *et al.*, 2015).

The output waveforms from the PIXIE ASIC were digitized and processed online by 16-channel digital electronics, developed at DiFC of the University of Palermo (Italy) (Abbene *et al.*, 2013*a,b*; Abbene & Gerardi, 2015; Gerardi & Abbene, 2014). The digital electronics are based on commercial digitizers (DT5724, 16 bit, 100 MS s^{-1}, CAEN SpA, Italy; http://www.caen.it), where an original firmware was uploaded (Abbene & Gerardi, 2015; Gerardi & Abbene, 2014). The digital analysis performs the shaping of the output waveform from the detector-ASIC using the classical single-delay line (SDL) shaping technique (Knoll, 2000). The delay time acts as the shaping time constant of a standard shaping amplifier. Moreover, to increase the signal-to-noise ratio (SNR) we also performed a further shaping with a trapezoidal filtering. Here we used a delay time of 200 ns. A detailed description of the digital analysis is reported in our previous works (Abbene & Gerardi, 2015; Gerardi & Abbene, 2014).
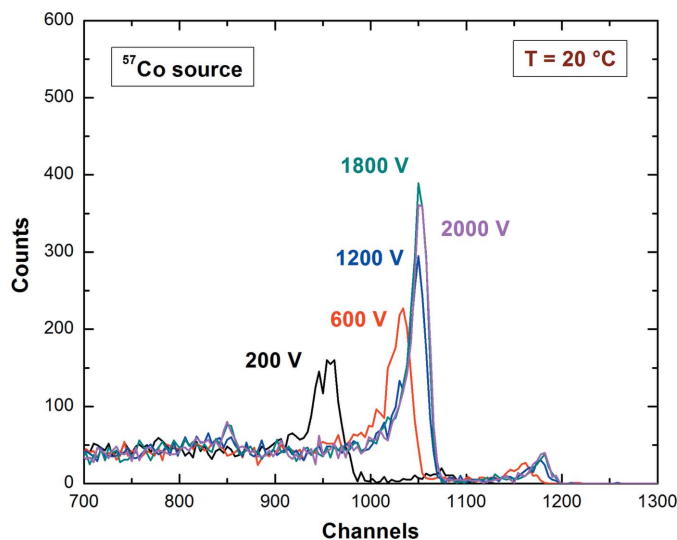
3. Experimental

Uncollimated radiation sources were used to characterize the detectors (^{109}Cd: 22.1 keV, 24.9 keV and 88.1 keV; ^{241}Am: 59.5 keV and 26.3 keV; ^{57}Co: 122.1 keV and 136.5 keV). The ^{57}Co energy spectra also feature W fluorescent lines produced in the tungsten source backing ($K\alpha_1 = 59.3$ keV, $K\alpha_2 = 58.0$ keV, $K\beta_1 = 67.2$ keV, $K\beta_3 = 66.9$ keV). The source holders shield the 14 keV gamma line of the ^{57}Co source and the Np *L*

X-ray lines of the [241]Am source. The detectors were irradiated through the cathode side and negative cathode bias voltages were applied. Collimated micro-beams were also used at the B16 test beamline at the Diamond Light Source synchrotron (Didcot, UK; http://www.diamond.ac.uk/Beamlines/ Materials/B16). All measurements were performed at room temperature (T = 20°C).

Table 1
Energy resolution FWHM at different energies with a bias voltage of 1800 V at T = 20°C.

The Fano noise was calculated using a Fano factor F = 0.1 (Devanathan *et al.*, 2006; Kuvvetli & Budtz-Jorgensen, 2005; Owens & Peacock, 2004).
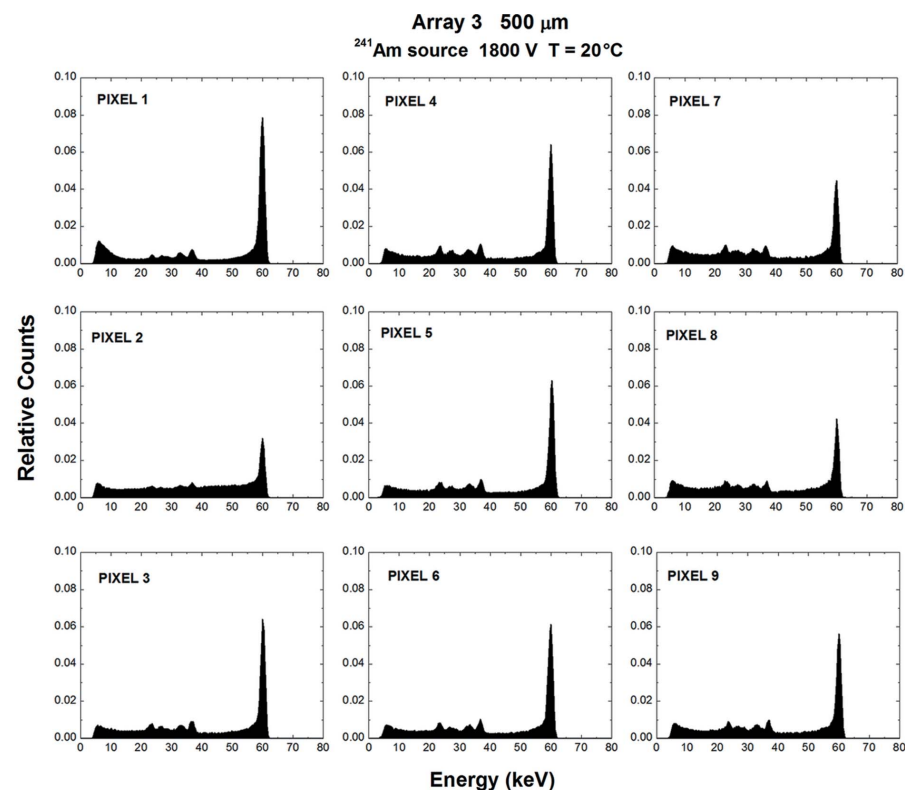
Array	Pixel	Energy resolution at 22.1 keV (keV) Fano noise: 0.2 keV	Energy resolution at 59.5 keV (keV) Fano noise: 0.4 keV	Energy resolution at 122.1 keV (keV) Fano noise: 0.6 keV
Array 3 (500 µm)	Best pixel (No. 3)	1.6 (7.3%)	1.7 (2.8%)	2.0 (1.6%)
Array 3 (500 µm)	Sum of all spectra	1.7 (7.8%)	1.8 (3%)	2.3 (1.9%)

4. Spectroscopic response of the detectors

Preliminary measurements involved investigations on the spectroscopic response of the detectors at different bias voltages. Fig. 2 shows the main photopeaks (122 keV and 136 keV) of the measured [57]Co energy spectra of a tested pixel of the large array (array 3: pixel pitch of 500 µm) at different cathode bias voltages, up to the electrical limits of the components of the bias voltage filters (2000 V). At room temperature, we obtained the best energy resolution of 1.6% (2 keV) full width at half-maximum (FWHM) at 122.1 keV at a bias voltage of 1800 V (6000 V cm^{-1}) (input counting rate ICR < 600 counts s^{-1}). This result highlights the high bias voltage operation of the detectors, strongly related to the good characteristics of the electrical contacts. Despite the quasi-ohmic contacts of the electrodes, the detectors allow low-leakage currents, as already shown in previous investigations with planar electrode structures (Abbene *et al.*, 2017*a*,*b*). Moreover, we stress that 3 mm-thick CZT pixel detectors did not typically exceed a cathode bias voltage of 1000 V at room temperature (Iwanczyk *et al.*, 2009; Jurdit *et al.*, 2017). An overview of the low-rate performance of the pixels of the

arrays is presented in Figs. 3 and 4. Despite the good room-temperature performance of the pixels of the large array, poor energy resolution characterizes the measured spectra of the pixels of the small array, as shown in Fig. 4. This can be attributed to the charge-sharing effects that are more severe for small pixels and when the gap-area-to-pixel area ratio is increased. The room-temperature energy resolution values are reported in Table 1.
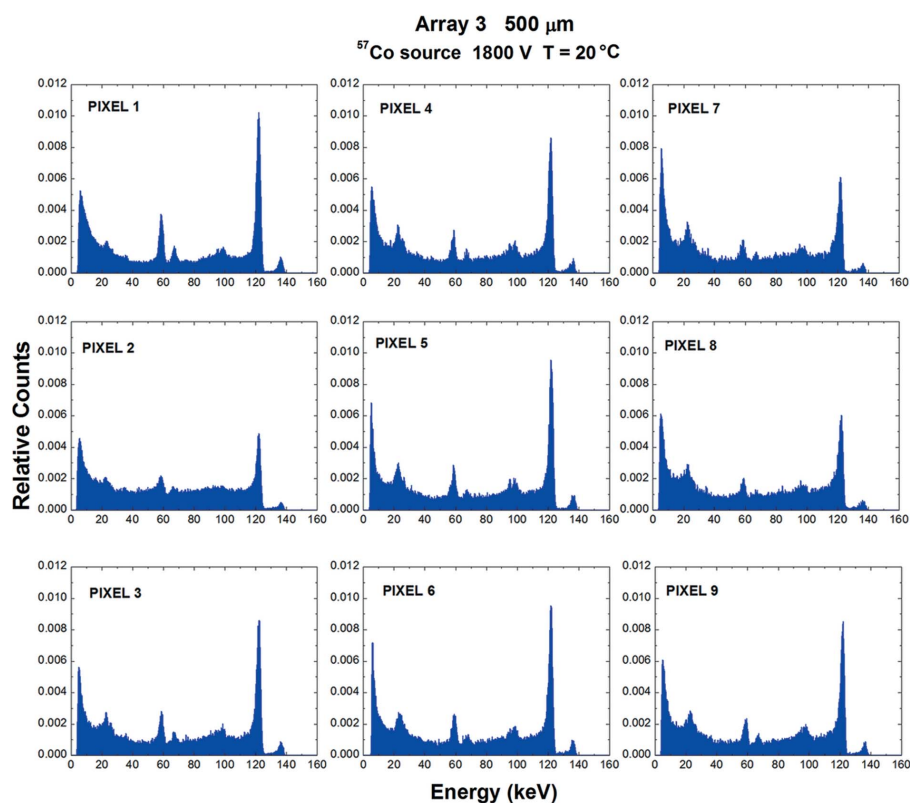
5. Charge-sharing measurements

Charge-sharing effects were also investigated. The shared events were analysed by detecting the events of a pixel which are in temporal coincidence – within a coincidence time window (CTW) – with the neighbouring pixels. This technique is generally termed time coincidence analysis (TCA). Aside from the charge-shared events, typically referred to as the splitting of the electron charge cloud generated from a single photon and collected by several pixels, cross-talk events can also be detected. These events are mainly created by K-shell fluorescence X-rays that can interact far from the interaction point below the collecting pixel (Xu *et al.*, 2011). Cross-talk events can be also produced by induced-charge pulses (Guerra *et al.*, 2008; Brambilla *et al.*, 2012; Bolotnikov *et al.*, 2016; Kim *et al.*, 2011; Zhu *et al.*, 2011). The induced-charge pulses (or transient pulses) are generated by movement of the electron cloud over a collecting pixel that will also induce a small signal on the surrounding non-collecting pixels (weighting potential cross-talk). A low number of these events were detected in our detectors, mainly in the [57]Co spectra. This is due to the low investigated energies (4–136 keV) that produce very small induced-charge pulses, often below the detection energy threshold (4 keV). Concerning our detectors, TCA measurements highlighted a high number of coincidence events in each pixel. For example, with uniform [241]Am source irradiation, the percentage of coincidence events of the central pixel with all eight adjacent pixels is 52% and 89% for the large and small arrays, respectively (detection energy threshold of 4 keV). These results stress that charge-sharing effects must be taken into account in sub-millimetre CZT pixel detectors; moreover, the high coincidence percentage for the small array justifies the poor spectroscopic performance of the pixels (Fig. 4). As is well known, coincidence events can be rejected from the raw energy spectra using the charge-sharing discrimination (CSD) technique. Fig. 5 shows the results after CSD for the measured [241]Am and [57]Co spectra. After CSD, the low-energy back-

Figure 2
Uncollimated [57]Co energy spectra of a selected pixel of the large array (array 3: 500 µm pixel pitch) at different cathode bias voltages. The best performance is obtained using a bias voltage of 1800 V, giving an energy resolution of 1.6% FWHM at 122.1 keV.

(a) Array 3 500 µm
^{241}Am source 1800 V T = 20°C


(b) Array 3 500 µm
^{57}Co source 1800 V T = 20 °C

Figure 3
Overview of the measured uncollimated (*a*) ^{241}Am and (*b*) ^{57}Co energy spectra of all nine pixels of large array 3 (500 µm) under low-rate conditions (ICR < 600 counts s^{-1}). The energy resolution (FWHM) of the best pixel (pixel 3) is 2.8% (1.7 keV) and 1.6% (2 keV) at 59.5 keV and 122.1 keV, respectively.

ground and the fluorescent X-ray events at 23.2 keV and 27.5 keV are removed and, concerning the ^{57}Co spectrum, the Compton edge at 39.5 keV is also clearly visible. No improvements in energy resolution were obtained after CSD, due to the non-zero energy threshold used in the sharing detection (4 keV). The critical issue of CSD is the strong reduction of the events in the spectra. To recover the rejected events after CSD, the charge-sharing addition (CSA) technique is typically applied. This simple approach consists of summing the energies of the coincidence events (E_{CSA}). However, as documented in the literature (Abbene *et al.*, 2015, 2018*a*; Allwork *et al.*, 2012; Brambilla *et al.*, 2012; Bolotnikov *et al.*, 1999, 2002; Gaskin *et al.*, 2003; Kalemci & Matteson, 2002; Kim *et al.*, 2011; Kuvvetli & Budtz-Jorgensen, 2007), the presence of charge losses at the inter-pixel gap of CdTe/CZT pixel detectors can create energy distortions in the measured spectra after CSA. Concerning our detectors, we observed charge/energy losses in the summed energy spectra after CSA (*i.e.* the E_{CSA} spectra). For example, as shown in Fig. 6, the main peak at 122.1 keV after CSA is characterized by an energy loss of about 4 keV. In order to exclude any ballistic deficit effect from the pulse processing, we estimated charge losses at different delay times (up to 10 µs), observing the same results. Charge losses after CSA are also present at other energies, showing a linear behaviour with the true photon energy. Generally, the interpretation of these charge losses is still debated. In recent years, several explanations have been proposed, such as (i) the non-zero energy threshold of the readout electronics (Kalemci & Matteson, 2002), (ii) the presence of electric field distortions at the inter-pixel gap (Bolotnikov *et al.*, 1999, 2002; Kuvvetli & Budtz-Jorgensen, 2007), (iii) the decreasing of weighting potential at the inter-pixel gap (Kim *et al.*, 2014) and (iv) the simultaneous presence of both the collected and the induced-charge components in the shared pulses between adjacent pixels (Bolotnikov *et al.*, 2016; Kim *et al.*, 2011).
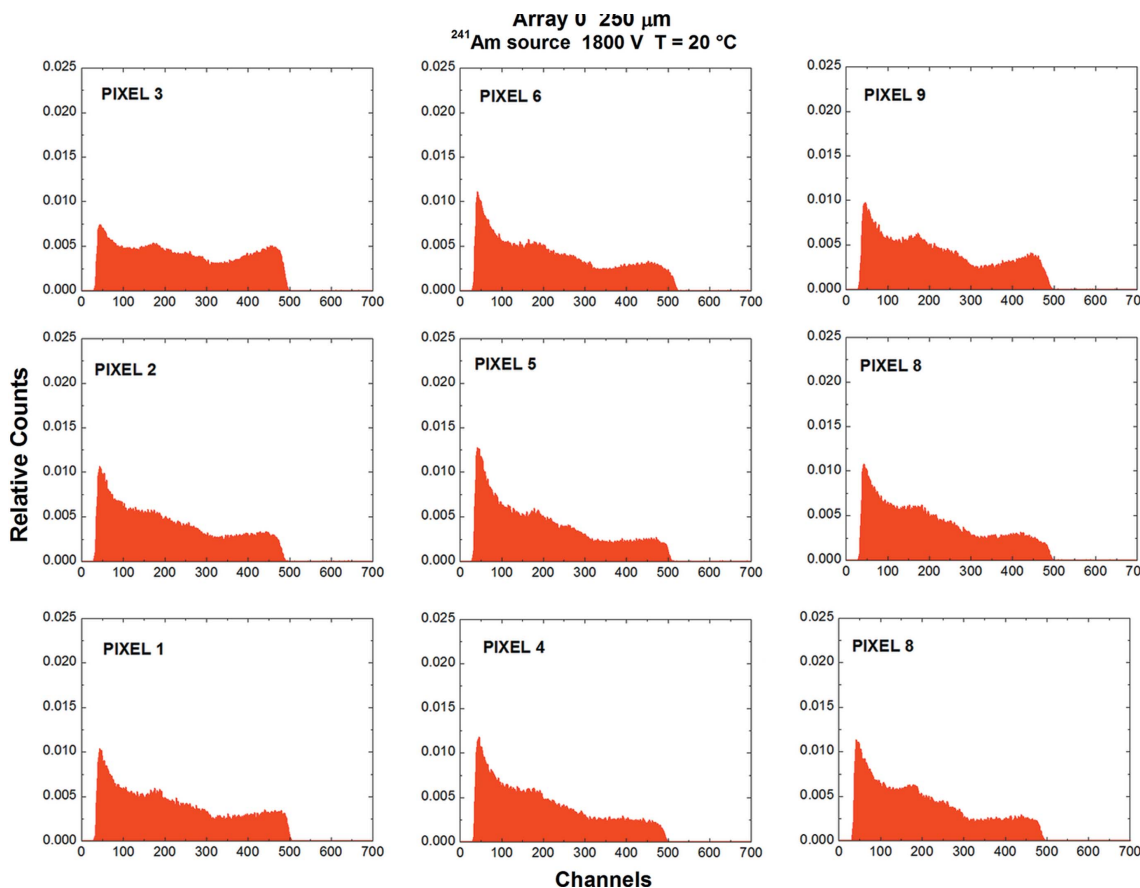
Figure 4
Uncollimated ^{241}Am energy spectra for the pixels of the small array (pixel pitch of 250 µm) at low-rate conditions (< 200 counts s^{-1}). The poor energy resolution of the measured spectra is caused by charge-sharing effects.

6. Sub-pixel characterization with collimated synchrotron X-rays

To better understand the effects of charge sharing, a micro-beam characterization of the detectors was also carried out. Investigations on a sub-pixel level were performed using collimated synchrotron X-rays. Fig. 7 shows the spectroscopic response of the detectors to mono-energetic synchrotron X-rays. In particular, we irradiated the centre of the pixel of both arrays with collimated X-ray beams (10 µm × 10 µm) at energies below (25 keV) and above (40 keV) the K-shell absorption energy of the CZT material (26.7 keV, 9.7 keV and 31.8 keV for Cd, Zn and Te, respectively). The photopeaks of the energy spectra are clearly visible even for the pixels of the small array. This confirms that the poor energy spectra obtained with uncollimated beams (Fig. 4) is mainly due to the photon interactions near the inter-pixel gaps which are strongly influenced by charge sharing. A microscale line scanning between the centres of two adjacent pixels (pixels 5 and 8) of the small array is presented. We used collimated (10 µm × 10 µm) synchrotron X-ray beams at 25 keV and 40 keV, with position steps of 10 µm. During the line scanning between two pixels, we acquired, at each beam position, the data from all nine pixels of the investigated array. Fig. 8 shows an overview of the variation of the photopeak centroid of the main peaks (25 keV and 40 keV) and the multiplicity m with
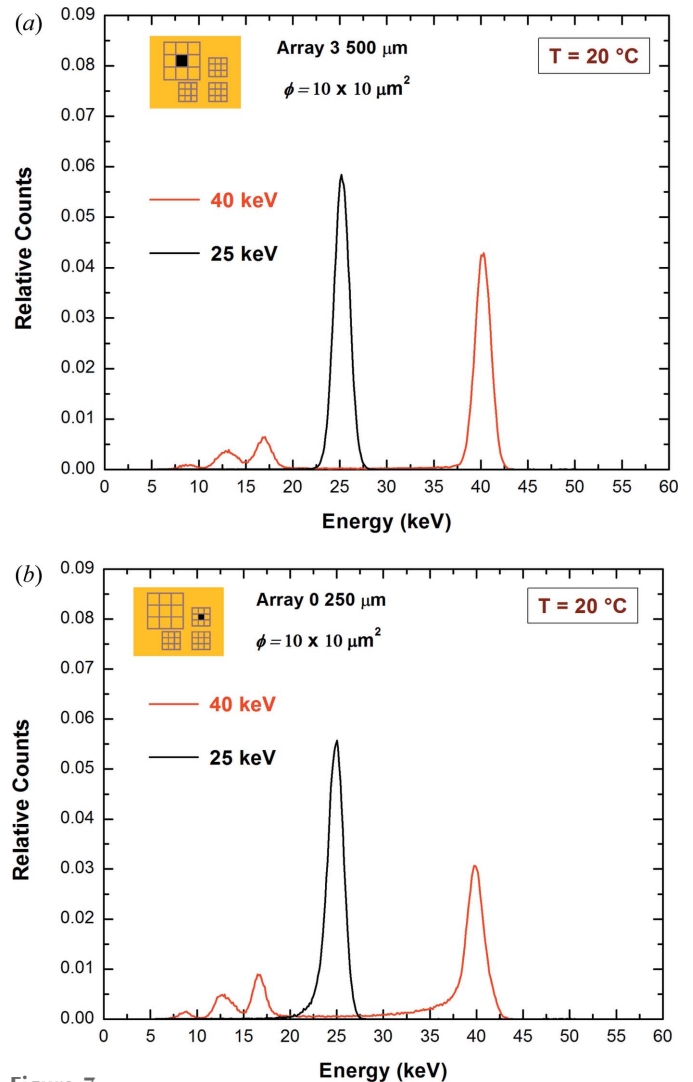
changing beam position. At 25 keV, centroid variations are observed in a region of 50 µm centred in the middle of the inter-pixel region. Coincidence events ($m > 1$) were only detected at beam positions within 50 µm of the centre of the inter-pixel region. At the centre of the inter-pixel gap almost 100% of events were shared between the two pixels. At 40 keV, coincidence events were detected in a wider region, even for beam positions near the centre of the pixels. This is due to the propagation of fluorescent X-rays which increases the initial charge cloud and creates cross-talk events. The attenuation lengths of the Cd $K\alpha$ and Cd $K\beta$ X-rays are 116 µm and 161 µm, respectively (Abbene *et al.*, 2018*a*; Allwork *et al.*, 2012).
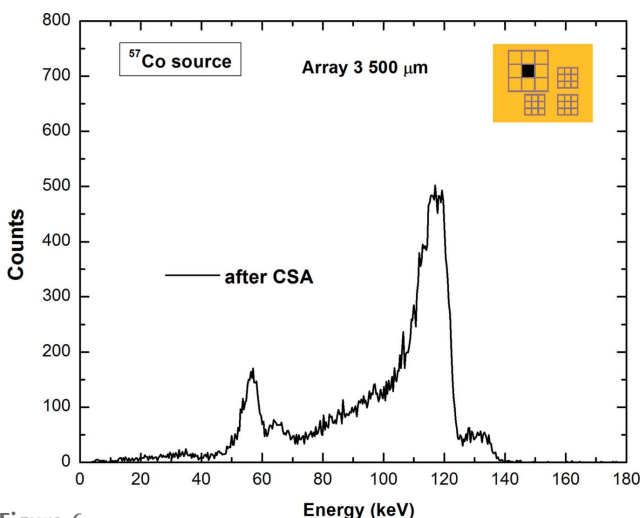
7. Charge-sharing correction

The presence of charge losses after CSA was also confirmed with collimated synchrotron X-ray beams. In particular, we presented the energy spectra at 25 keV for a collimated beam position at the centre of the inter-pixel gap, where charge sharing is more severe. Fig. 9(*a*) shows a 2D scatter plot of the energy E_{CSA} of the coincidence events ($m = 2$) after CSA, between pixels 5 and 4, versus the charge-sharing ratio R, at the centre of the inter-pixel gap. The presence of charge losses at 25 keV allows us to exclude the detection energy threshold
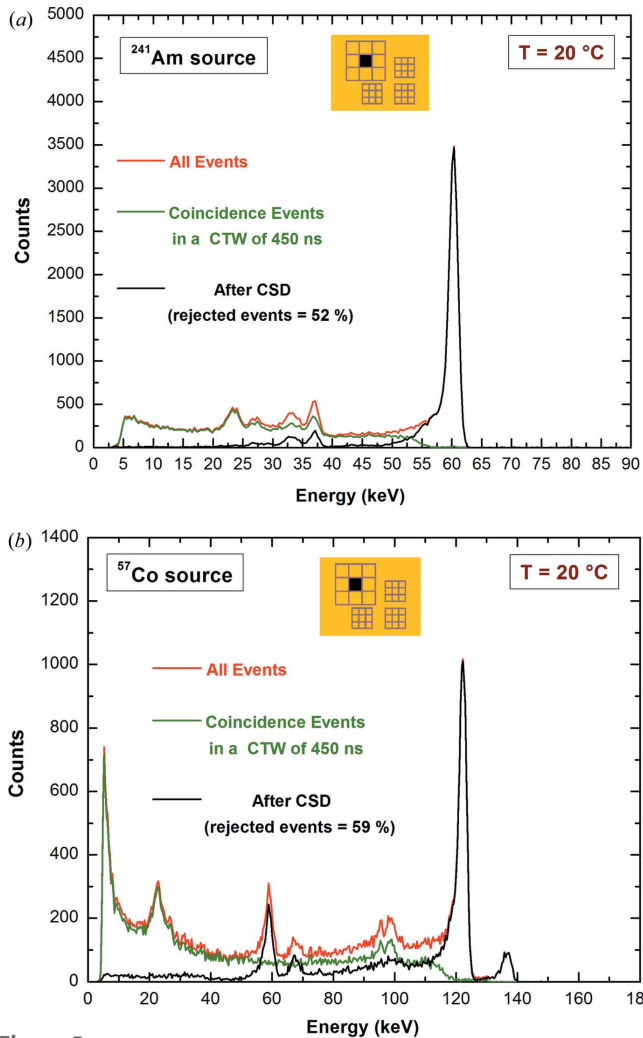
Figure 5
Measured (a) ^{241}Am and (b) ^{57}Co spectra of the central pixel of the large array after CSD (black line). The raw spectra of the central pixel (red line) and the spectra of the coincidence events with all eight adjacent pixels (green line) are shown. Energy resolution (FWHM) did not improve after CSD (1.9 keV at 59.5 keV and 2.4 keV at 122.1 keV).
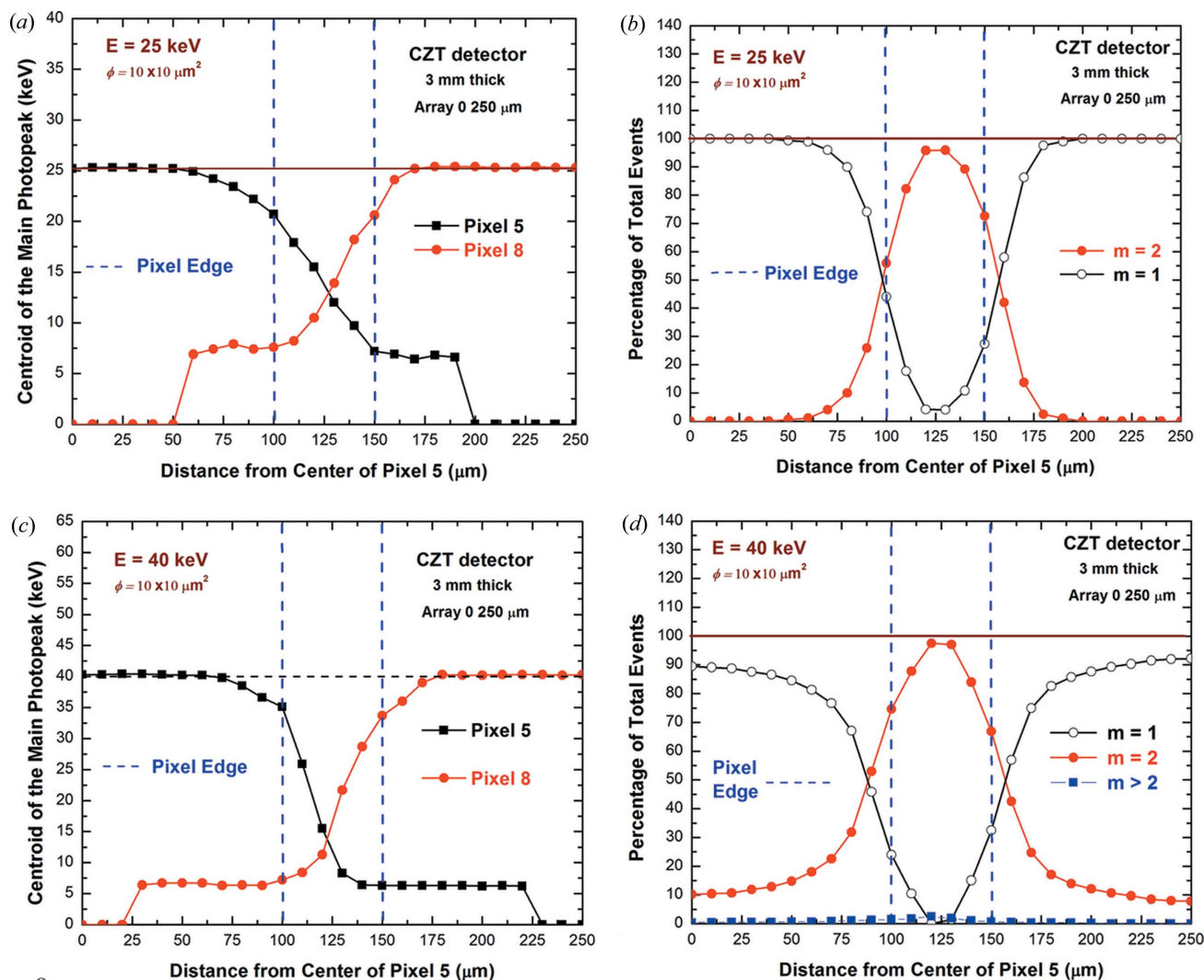

Figure 6
^{57}Co spectrum of the summed energy of coincidence events among the central pixel and eight adjacent pixels, *i.e.* the coincidence spectrum after CSA or the E_{CSA} spectrum. Charge losses after CSA are clearly visible.

Figure 7
Measured energy spectra to mono-energetic synchrotron X rays collimated ($\phi = 10\,\mu m \times 10\,\mu m$) at the centre of the central pixel of (a) large and (b) small arrays. Energy spectra at 25 keV and at 40 keV are presented. The energy resolution values (FWHM) are 1.8 keV and 2.0 keV for the large and small arrays, respectively.

of the electronics as the possible cause of charge losses. As presented in previous works (Abbene *et al.*, 2018b; Bugby *et al.*, 2019), the energy losses, clearly highlighted by the curvature of Fig. 9(a), can be recovered using a function which fits the experimental 2D scatter plot [Fig. 9(a)]. Different energy spectra of pixel 5 are presented in Fig. 9(b): the raw spectrum (black line), the energy spectrum after CSA (blue line) and after charge-sharing correction (CSC) with the fitting function (red line). This technique was applied for coincidence events with m = 2. A detailed description of this correction technique is reported in previous work (Abbene *et al.*, 2018b). Energy spectra at 40 keV are also presented in Fig. 10: the raw spectra at the centre on the inter-pixel gap and the spectra after CSC. The results are very impressive: charge sharing is correctly detected and the charge losses after CSA are fully recovered. As a comparison, the energy resolution of the central pixel at 25 keV is 1.8 keV [Fig. 7(a)] and 3.0 keV [Fig. 9(b)] at the

Figure 8
Microscale line scanning (10 µm position steps) between the centres of two adjacent pixels (pixels 5 and 8) at energies below (25 keV) and above (40 keV) the *K*-shell absorption energy of CZT material. (*a*) and (*c*) Photopeak centroids and (*b*) and (*d*) multiplicity *m* at various beam positions. The jump discontinuities visible in the curves for peak centroid values around 6 keV are the result of the non-zero energy threshold (4 keV).
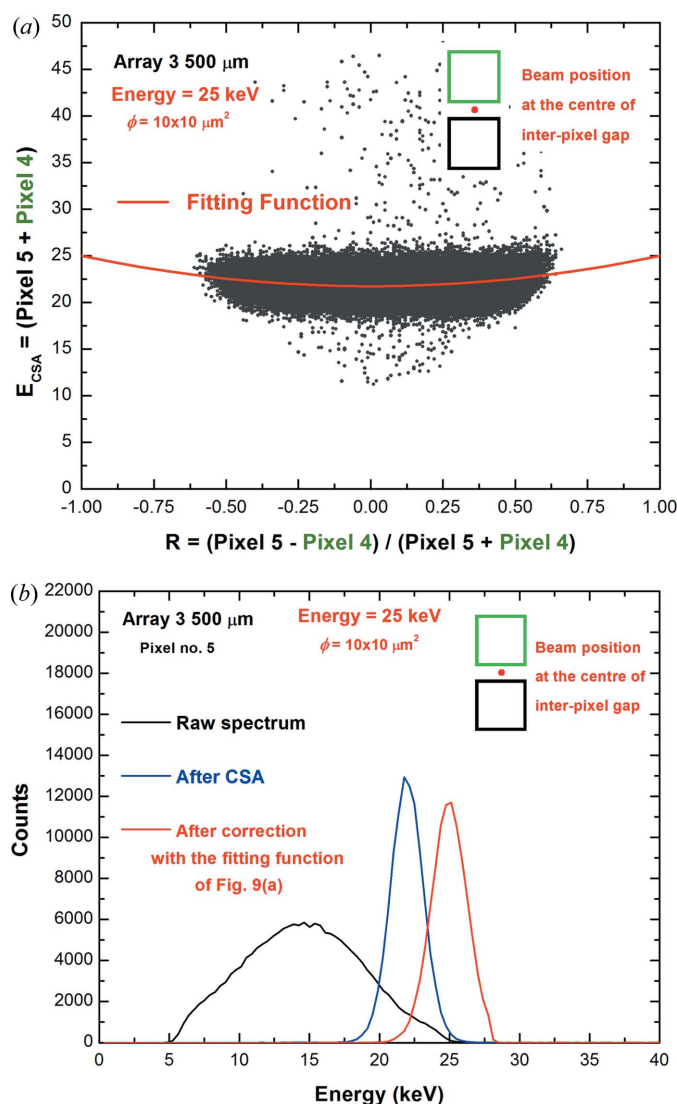
centre of the pixel and at the centre of the inter-pixel gap (after CSC), respectively. Despite the low energy resolution obtained after CSC, we stress that the correction was applied at the centre of the inter-pixel gap where charge losses are more severe. In other photon positions, where charge losses are less severe, better recovering was obtained as shown with uncollimated radiation sources (Fig. 11). In this case, the coincidence events with multiplicity *m* > 2 were also recovered. The effects of charge sharing are successfully mitigated and the corrected spectra after CSC show very low degradation of the energy resolution with a full recovery of the coincidence events. For example, the energy resolution (FWHM) at 122 keV is 1.9% and 2.3% for the raw and corrected spectra, respectively.

8. High rate measurements

The spectroscopic response of the detectors was also measured at high-rate conditions. The aim was to investigate

the presence of high-flux radiation polarization effects in the detectors (Abbene *et al.*, 2016; Bale & Szeles, 2008). Typically, high fluxes produce a charge build-up within the detectors which collapses the electric field and produces strong distortions in charge collection. This effect is mainly attributed to the poor charge transport properties of the holes (hole mobility-lifetime product $\mu_h \tau_h < 10^{-5}$ cm^2 V^{-1}) and, therefore, a careful choice of both crystal and device properties (electrode contact, bias voltage, thickness) is necessary to mitigate these effects. Synchrotron X-ray spectra at 40 keV were measured at different rates (Fig. 12) by irradiating a pixel area of 400 µm × 40 µm. The measured spectra show no energy shifts and low spectroscopic degradation up to 400 kcounts s^{-1}; this can mainly be attributed to the high-rate ability of the digital electronics, which minimize both the baseline shift and the peak pile-up effects in the spectra. However, no polarization effects were observed up to the investigated fluence rate conditions (25×10^6 photons mm^{-2} s^{-1}).
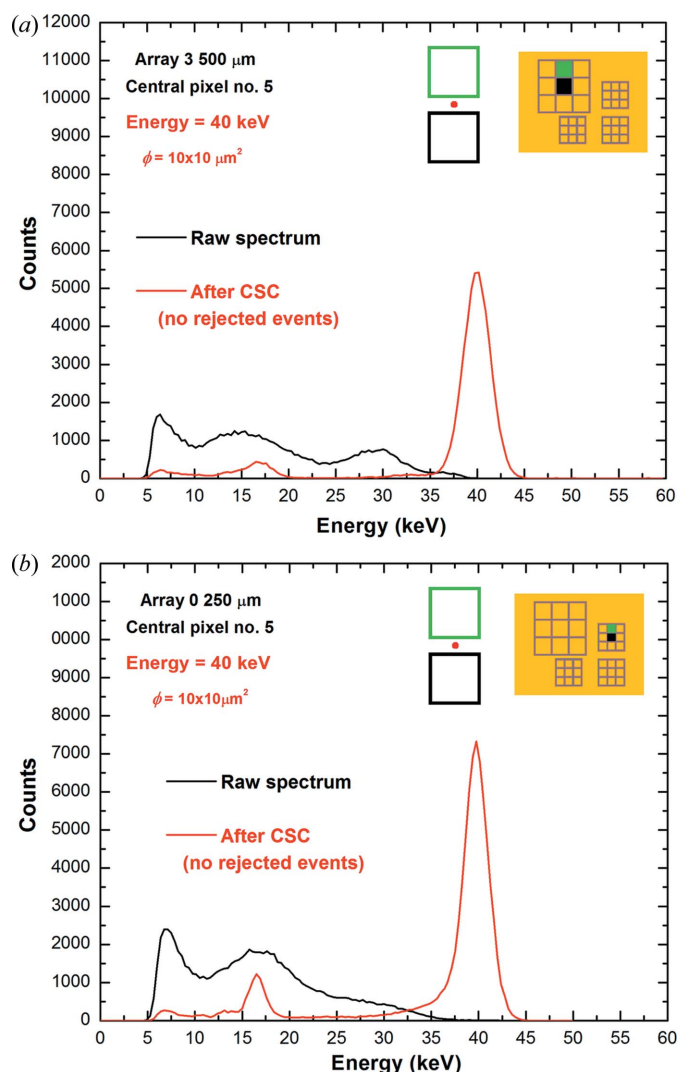
Figure 9
(a) 2D scatter plot of the energy E_{CSA} of the coincidence events ($m = 2$) between pixels 5 and 4 for a photon interaction at the centre of the inter-pixel gap. The energy E_{CSA} is plotted versus the charge-sharing ratio R, which provides information about the interaction position of the events. The red line represents the best fitting function used to correct charge losses after CSA. (b) The raw spectrum of pixel 5 (black line), the energy spectrum after CSA (blue line) and the spectrum after the proposed correction technique (red line) with the fitting function of Fig. 9(a). The energy resolution after CSC is equal to 3.0 keV.

9. Conclusions

New CZT pixel detectors with sub-millimetre pixelization (pixel pitches of 500 μm and 250 μm) were fabricated at IMEM/CNR of Parma, Italy. The detectors show good room-temperature performance at high bias voltage conditions (6000 V cm^{-1} electric field), with energy resolution values less than 2 keV up to 140 keV. Charge-sharing measurements, with uncollimated and collimated beams, highlighted high sharing percentages and the presence of charge losses near the inter-pixel gaps. CSC was successfully applied with the full recovery of charge losses. The absence of high-flux radiation-induced polarization effects was also observed up to photon fluence rates of 25×10^6 photons mm^{-2} s^{-1}.

Figure 10
Raw energy spectra (black lines) of the central pixel for the photon interaction at the centre of the inter-pixel gap for (a) the large and (b) the small arrays. The corrected spectra (red lines), i.e. after CSC, are also shown. The energy resolution FWHM after CSC is 3.0 keV for both arrays.
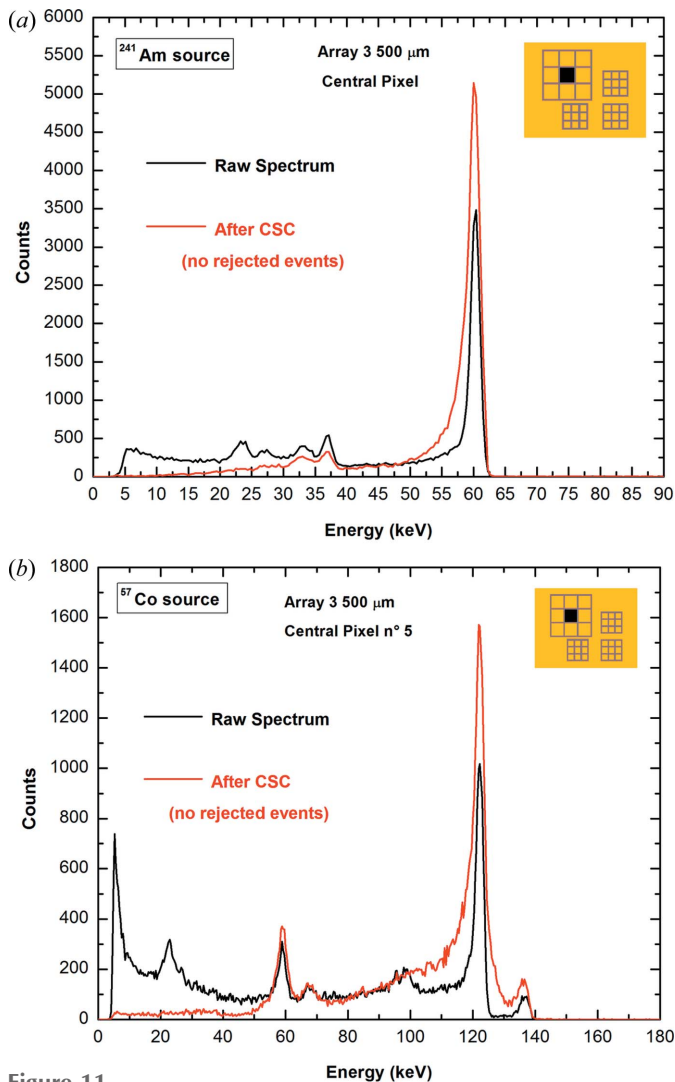
Figure 11
Raw energy spectra (black lines) of the central pixel to uncollimated (*a*) [241]Am and (*b*) [57]Co sources. The corrected spectra (red lines), *i.e.* after CSC, are also shown, with the full recovering of all coincidence events with low-energy resolution degradation.
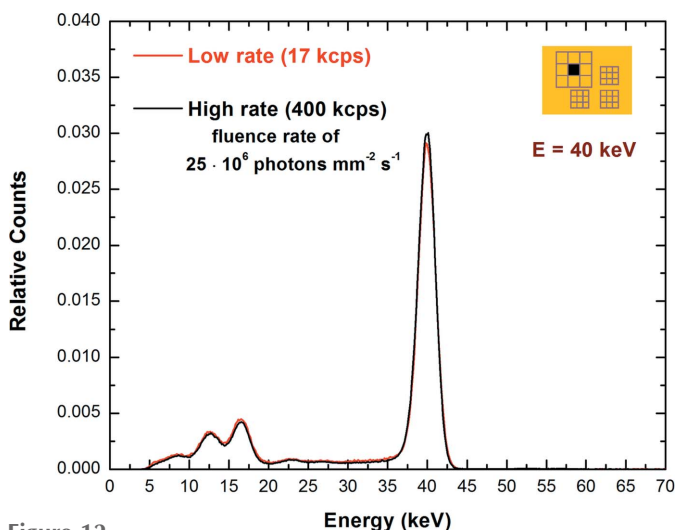
Figure 12
Measured synchrotron X-ray spectra of the central pixel of the large array at different ICRs.

References

Abbene, L. *et al.* (2017*b*). *IEEE Nucl. Sci. Symp. Conf. Rec.* 8069962.

Abbene, L. & Gerardi, G. (2015). *J. Synchrotron Rad.* **22**, 1190–1201.

Abbene, L., Gerardi, G. & Principato, F. (2013*a*). *Nucl. Instrum. Methods Phys. Res. A*, **730**, 124–128.

Abbene, L., Gerardi, G. & Principato, F. (2015). *Nucl. Instrum. Methods Phys. Res. A*, **777**, 54–62.

Abbene, L., Gerardi, G., Principato, F., Bettelli, M., Seller, P., Veale, M. C., Fox, O., Sawhney, K., Zambelli, N., Benassi, G. & Zappettini, A. (2018*b*). *J. Synchrotron Rad.* **25**, 1078–1092.

Abbene, L., Gerardi, G., Raso, G., Principato, F., Zambelli, N., Benassi, G., Bettelli, M. & Zappettini, A. (2017*a*). *J. Synchrotron Rad.* **24**, 429–438.

Abbene, L., Gerardi, G., Turturici, A. A., Del Sordo, S. & Principato, F. (2013*b*). *Nucl. Instrum. Methods Phys. Res. A*, **730**, 135–140.

Abbene, L., Gerardi, G., Turturici, A. A., Raso, G., Benassi, G., Bettelli, M., Zambelli, N., Zappettini, A. & Principato, F. (2016). *Nucl. Instrum. Methods Phys. Res. A*, **835**, 1–12.

Abbene, L., Principato, F., Gerardi, G., Bettelli, M., Seller, P., Veale, M. C., Zambelli, N., Benassi, G. & Zappettini, A. (2018*a*). *J. Synchrotron Rad.* **25**, 257–271.

Abbene, L., Principato, F., Gerardi, G., Buttacavoli, A., Cascio, D., Bettelli, M., Amadè, N. S., Seller, P., Veale, M. C., Fox, O., Sawhney, K., Zanettini, S., Tomarchio, E. & Zappettini, A. (2020). *J. Synchrotron Rad.* **27**, 319–328.

Allwork, C., Kitou, D., Chaudhuri, S., Sellin, P. J., Seller, P., Veale, M. C., Tartoni, N. & Veeramani, P. (2012). *IEEE Trans. Nucl. Sci.* **59**, 1563–1568.

Awadalla, S. A., Al-Grafi, M. & Iniewski, K. (2014). *Nucl. Instrum. Methods Phys. Res. A*, **764**, 193–197.

Bale, D. S. & Szeles, C. (2008). *Phys. Rev. B*, **77**, 035205.

Barber, W. C., Wessel, J. C., Nygard, E. & Iwanczyk, J. S. (2015). *Nucl. Instrum. Methods Phys. Res. A*, **784**, 531–537.

Bell, S. J., Baker, M. A., Duarte, D. D., Schneider, A., Seller, P., Sellin, P. J., Veale, M. C. & Wilson, M. D. (2015). *J. Phys. D Appl. Phys.* **48**, 275304.

Benassi, G., Nasia, L., Bettellia, M., Zambelli, N., Calestania, D. & Zappettinia, A. (2017). *J. Instrum.* **12**, P02028.

Bolotnikov, A. E., Boggs, S. E., Hubert Chen, C. M., Cook, W. R., Harrison, F. A. & Schindler, S. M. (2002). *Nucl. Instrum. Methods Phys. Res. A*, **482**, 395–407.

Bolotnikov, A. E., Camarda, G. S., Cui, Y., De Geronimo, G., Eger, J., Emerick, A., Fried, J., Hossain, A., Roy, U., Salwen, C., Soldner, S., Vernon, E., Yang, G. & James, R. B. (2016). *Nucl. Instrum. Methods Phys. Res. A*, **805**, 41–54.

Bolotnikov, A. E., Cook, W. R., Harrison, F. A., Wong, A., Schindler, S. M. & Eichelberger, A. C. (1999). *Nucl. Instrum. Methods Phys. Res. A*, **432**, 326–331.

Brambilla, A., Ouvrier-Buffet, P., Gonon, G., Rinkel, J., Moulin, V., Boudou, C. & Verger, L. (2013). *IEEE Trans. Nucl. Sci.* **60**, 408–415.

Brambilla, A., Ouvrier-Buffet, P., Rinkel, J., Gonon, G., Boudou, C. & Verger, L. (2012). *IEEE Trans. Nucl. Sci.* **59**, 1552–1558.

Bugby, S. L., Koch-Mehrin, K. A., Veale, M. C., Wilson, M. D. & Lees, J. E. (2019). *Nucl. Instrum. Methods Phys. Res. A*, **940**, 142–151.

Chen, H., Awadalla, S. A., Iniewski, K., Lu, P. H., Harris, F., Mackenzie, J., Hasanen, T., Chen, W., Redden, R., Bindley, G., Kuvvetli, I., Budtz-Jørgensen, C., Luke, P., Amman, M., Lee, J. S., Bolotnikov, A. E., Camarda, G. S., Cui, Y., Hossain, A. & James, R. B. (2008). *J. Appl. Phys.* **103**, 014903.

Del Sordo, S., Strazzeri, M., Agnetta, G., Biondo, B., Celi, F., Guarrusso, S., Mangano, A., Russo, F., Caroli, E., Donati, A., Schiavone, F., Stephen, J. B., Ventura, G., Abbene, L., Fauci, F., Raso, G. & Pareachi, G. (2004). *Nuovo Cimento B*, **119**, 257–270.

Del Sordo, S., Abbene, L., Caroli, E., Mancini, A. M., Zappettini, A. & Ubertini, P. (2009). *Sensors*, **9**, 3491–3526.

Del Sordo, S., Abbene, L., Zora, M., Agnetta, G., Biondo, B., Mangano, A., Russo, F., Caroli, E., Auricchio, N., Donati, A., Schiavone, F., Stephen, J. B., Ventura, G., Bertuccio, G., Caccia, S. & Sampietro, M. (2005). *IEEE Trans. Nucl. Sci.* **52**, 3091–3095.

Devanathan, R., Corrales, L. R., Gao, F. & Weber, W. J. (2006). *Nucl. Instrum. Methods Phys. Res. A*, **565**, 637–649.

Farella, I., Montagna, G., Mancini, A. M. & Cola, A. (2009). *IEEE Trans. Nucl. Sci.* **56**, 1736–1742.

Gaskin, J. A., Sharma, D. P. & Ramsey, B. D. (2003). *Nucl. Instrum. Methods Phys. Res. A*, **505**, 122–125.

Gerardi, G. & Abbene, L. (2014). *Nucl. Instrum. Methods Phys. Res. A*, **768**, 46–54.

Guerra, P., Santos, A. & Darambara, D. G. (2008). *Phys. Med. Biol.* **53**, 1099–1113.

Iniewski, K. (2014). *J. Instrum.* **9**, C11001.

Iwanczyk, J., Nygård, E., Meirav, O., Arenson, J., Barber, W. C., Hartsough, N. E., Malakhov, N. & Wessel, J. C. (2009). *IEEE Trans. Nucl. Sci.* **56**, 535–542.

Johns, P. M. & Nino, J. C. (2019). *J. Appl. Phys.* **126**, 040902.

Jurdit, M., Brambilla, A., Moulin, V., Ouvrier-Buffet, P., Radisson, P. & Verger, L. (2017). *J. Instrum.* **12**, T09008.

Kalemci, E. & Matteson, J. L. (2002). *Nucl. Instrum. Methods Phys. Res. A*, **478**, 527–537.

Kim, J. C., Anderson, S. E., Kaye, W., Zhang, F., Zhu, Y., Kaye, S. J. & He, Z. (2011). *Nucl. Instrum. Methods Phys. Res. A*, **654**, 233–243.

Kim, J. C., Kaye, W. R. & He, Z. (2014). *J. Korean Phys. Soc.* **64**, 1336–1345.

Knoll, G. F. (2000). *Radiation Detection and Measurement*. New York: John Wiley.

Kuvvetli, I. & Budtz-Jorgensen, C. (2005). *IEEE Trans. Nucl. Sci.* **52**, 1975–1981.

Kuvvetli, I. & Budtz-Jorgensen, C. (2007). *IEEE Nucl. Sci. Symp. Conf. Rec.* **3**, 2252–2257.

Marchini, L., Zappettini, A., Gombia, E., Mosca, R., Lanata, M. & Pavesi, M. (2009). *IEEE Trans. Nucl. Sci.* **56**, 1823–1826.

Owens, A. & Peacock, A. (2004). *Nucl. Instrum. Methods Phys. Res. A*, **531**, 18–37.

Principato, F., Turturici, A. A., Gallo, M. & Abbene, L. (2013). *Nucl. Instrum. Methods Phys. Res. A*, **730**, 141–145.

Prokesch, M., Soldner, S. A. & Sundaram, A. G. (2018). *J. Appl. Phys.* **124**, 044503.

Schneider, A., Veale, M. C., Duarte, D. D., Bell, S. J., Wilson, M. D., Lipp, J. D. & Seller, P. (2015). *J. Instrum.* **10**, C02010.

Szeles, C., Soldner, S. A., Vydrin, S., Graves, J. & Bale, D. S. (2008). *IEEE Trans. Nucl. Sci.* **55**, 572–582.

Takahashi, T. & Watanabe, S. (2001). *IEEE Trans. Nucl. Sci.* **48**, 950–959.

Turturici, A. A., Abbene, L., Gerardi, G. & Principato, F. (2014). *Nucl. Instrum. Methods Phys. Res. A*, **763**, 476–482.

Veale, M. C., Booker, P., Cross, S., Hart, M. D., Jowitt, L., Lipp, J., Schneider, A., Seller, P., Wheater, R. M., Wilson, M. D., Hansson, C. C. T., Iniewski, K., Marthandam, P. & Prekas, G. (2020). *Sensors*, **20**, 2747.

Veale, M. C., Bell, S. J., Jones, L. L., Seller, P., Wilson, M. D., Allwork, C., Kitou, D., Sellin, P. J., Veeramani, P. & Cernik, R. C. (2011). *IEEE Trans. Nucl. Sci.* **58**, 2357–2362.

Xu, C., Danielsson, M. & Bornefalk, H. (2011). *IEEE Trans. Nucl. Sci.* **58**, 614–625.

Zappettini, A., Zha, M., Marchini, L., Calestani, D., Mosca, R., Gombia, E., Zanotti, L., Zanichelli, M., Pavesi, M., Auricchio, N. & Caroli, E. (2009). *IEEE Trans. Nucl. Sci.* **56**, 1743–1746.

Zhu, Y., Anderson, S. E. & He, Z. (2011). *IEEE Trans. Nucl. Sci.* **58**, 1400–1409.